THE JOURNAL OF PHYSICAL CHEMISTRY Letters

pubs.acs.org/JPCL Letter

Minimizing the Trade-Off between Photocurrent and Photovoltage in Triple-Cation Mixed-Halide Perovskite Solar Cells

Thomas Baumeler, Neha Arora, Alexander Hinderhofer, Seckin Akin, Alessandro Greco, Mojtaba Abdi-Jalebi, Ravichandran Shivanna, Ryusuke Uchida, Yuhang Liu, Frank Schreiber, Shaik M. Zakeeruddin, Richard H. Friend, Michael Graetzel, and M. Ibrahim Dar*

Cite This: *J. Phys. Chem. Lett.* 2020, 11, 10188−10195 Read Online

ACCESS | Metrics & More | Article Recommendations | Supporting Information

ABSTRACT: Its lower bandgap makes formamidinium lead iodide ($FAPbI_3$) a more suitable candidate for single-junction solar cells than pure methylammonium lead iodide ($MAPbI_3$). However, its structural and thermodynamic stability is improved by introducing a significant amount of MA and bromide, both of which increase the bandgap and amplify trade-off between the photocurrent and photovoltage. Here, we simultaneously stabilized $FAPbI_3$ into a cubic lattice and minimized the formation of photoinactive phases such as hexagonal $FAPbI_3$ and PbI_2 by introducing 5% $MAPbBr_3$, as revealed by synchrotron X-ray scattering. We were able to stabilize the composition $(FA_{0.95}MA_{0.05}Cs_{0.05})Pb(I_{0.95}Br_{0.05})_3$, which exhibits a minimal trade-off between the photocurrent and photovoltage. This material shows low energetic disorder and improved charge-carrier dynamics as revealed by photothermal deflection spectroscopy (PDS) and transient absorption spectroscopy (TAS), respectively. This allowed the fabrication of operationally stable perovskite solar cells yielding reproducible efficiencies approaching 22%.

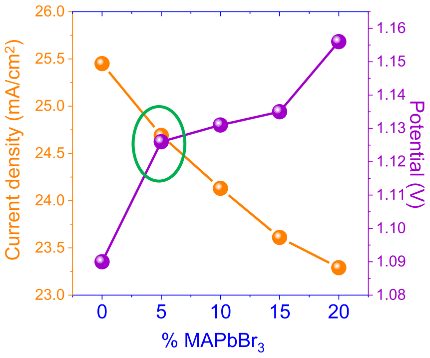

Hybrid perovskite materials exhibit the ABX_3 structure, where A generally stands for a monovalent cation such as methylammonium (MA) = $CH_3NH_3^+$, cesium (Cs^+), or formamidinium (FA) = $CH(NH_2)_2^+$, B stands for a divalent metal cation (Pb^{2+}, Sn^{2+}), and X stands for a monovalent halide anion (I^-, Br^-, Cl^-).[1−3] These perovskite semiconductors exhibit outstanding optoelectronic properties, including a high absorption coefficient over a wide range of the solar spectral irradiance, a direct bandgap, low exciton binding energy, large charge-carrier diffusion lengths, and ambipolarity.[4−8]

Initially, Kojima et al. demonstrated $MAPbBr_3$ and $MAPbI_3$ perovskite materials for photovoltaic applications.[1] With the substitution of bromide by iodide, the bandgap decreases and the spectral sensitivity toward longer wavelengths (up to 800 nm) increases, leading to the amplification of short-circuit photocurrent (J_{sc}) but reducing the open-circuit photovoltage (V_{oc}).[9] This tunability feature of perovskite materials was further extended to the A-site cation by Koh et al., who demonstrated $FAPbI_3$ perovskite as a potential light absorber with a bandgap of 1.47 eV.[10] Although a low bandgap makes $FAPbI_3$ a more desired light absorber, the thermodynamic instability of the photoactive trigonal black phase of $FAPbI_3$ (α-$FAPbI_3$) under ambient conditions poses a serious challenge to materials scientists and the photovoltaics community. To address this issue, different strategies have been identified by the scientific community. For example, methylammonium chloride-induced stabilization of α-$FAPbI_3$ phase,[11] and surface coating via a molecularly tailored two-dimensional (2D) overlayer rendering the back conversion of α-$FAPbI_3$ to δ-$FAPbI_3$ less favorable has been reported recently.[12]

At the beginning, Pellet et al. stabilized the photoactive phase by mixing MA and FA cations to form multication $MA_xFA_{1-x}PbI_3$ perovskites.[13] In a similar direction, Jeon et al. reasoned that the incorporation of $MAPbBr_3$ into $FAPbI_3$ stabilizes the perovskite phase of latter and simultaneously improves the power conversion efficiency (PCE) of the perovskite solar cells (PSCs).[14] Subsequently, the compositional engineering of perovskite materials attracted tremendous attention to developing highly efficient and stable PSCs.[15−24] By introducing Cs^+ cation into $(FAMA)PbX_3$ perovskite structures, further improvement in the thermal stability and reduction in phase impurities was shown.[25,26] The resulting state-of-the-art triple-cation perovskite composition contains >15% of $MAPbBr_3$ in an FA-dominant lattice exhibiting a bandgap of 1.63 eV, which is larger than that of pure

Received: September 12, 2020
Accepted: October 23, 2020

https://dx.doi.org/10.1021/acs.jpclett.0c02791
J. Phys. Chem. Lett. 2020, 11, 10188−10195

$MAPbI_3$.[14] Therefore, optimization of $MAPbBr_3$ content within the $FAPbI_3$ perovskite structure is critical, primarily, to minimize the trade-off between the photocurrent and photovoltage, which can consequently enhance the PCE of resulting PSCs. Arguably, this will lead to the fabrication of more efficient devices, which will pave the way toward stable and reproducible devices, a key factor toward the industrialization of PSCs.[11]

Herein, we aimed to minimize the $MAPbBr_3$ content in order to ensure high PCE while still benefiting from the stability features of $MAPbBr_3$. We probed the PCE and stability of PSCs in order to find out the composition, which demonstrates the best compromise between the stabilization features and the loss of photocurrent associated with $MAPbBr_3$, while simultaneously improving the overall photovoltaic performance of FA-dominant PSCs.

We deposited $CsI_{0.05}(FA_{1-y}MA_y)_{0.95}Pb(I_{1-y}Br_y)_3$ (y = 0, 0.05, 0.10, 0.15, 0.20) (denoted as P + y% $MAPbBr_3$) perovskite films using the one-step solution-based antisolvent method. See the experimental methods for further details.

To investigate the composition of perovskite films and to establish the effectiveness of the experimental methodology, we explored X-ray photoelectron spectroscopy (XPS). As shown in Figure S1 and Table S1, Pb and Cs experimental concentrations are relatively stable across the series while the iodide and bromide concentrations follow the expected trend. The relative contents of halides determined from the XPS data correlate with the values calculated for each condition (Table S1), which confirms the effective introduction of the desired amounts of $MAPbBr_3$ into the CsI-containing $FAPbI_3$ perovskite lattice system. Nevertheless, the presence of undesired phases that could influence the final composition of the 3D perovskite needs to be considered. In addition, the peaks attributed to lead (Pb $4f_{5/2}$ and Pb $4f_{7/2}$), iodide (I $3d_{3/2}$ and I $3d_{5/2}$), and bromide (Br $3d_{3/2}$ and Br $3d_{5/2}$) display a shift, which could be associated with the binding energy as a function of composition.[27−29]

The effect of perovskite composition on the morphology and thickness of the film was investigated through field-emission scanning electron microscopy (FE-SEM) (Figure 1, Figures S2−S4). Top view SEM micrographs reveal that $MAPbBr_3$-free perovskite film (Figure 1A) is composed of submicron-sized structures, while with the introduction of 5% $MAPbBr_3$, the grain size decreases dramatically to ~200−300 nm (Figure 1B) and remains invariant with $MAPbBr_3$ concentration (Figure 1E). Such growth behavior can be explained by invoking an increase in the nucleation density induced by $MAPbBr_3$ (Figure 1C,D). Cross-sectional SEM reveals that the composition insignificantly influences the perovskite film thickness as all the $MAPbBr_3$-containing perovskite film exhibit a thickness of approximately 500 nm (Figure 1F).

To gain deeper insight into the growth and formation of the perovskite structures, we recorded grazing-incidence X-ray scans[30] of the perovskite film samples containing different mixtures of $MAPbBr_3$ and $FAPbI_3$. In addition to peaks corresponding to the perovskite phase, we also observed the features that can be attributed to the hexagonal (yellow) $FAPbI_3$ phase and lead iodide (Figure 2A). By fitting the perovskite peaks with a Gaussian, we determined the peak position as well as the width of each peak (Figure 2B). Assuming a cubic perovskite structure, an average lattice parameter was determined. Figure 2C shows that the average lattice parameter depends linearly on the amount of added

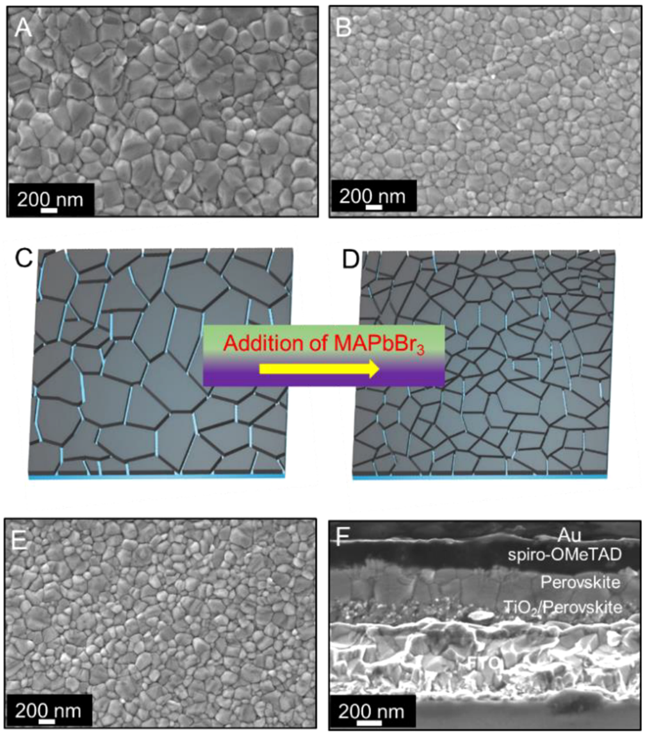

Figure 1. Morphological analysis of perovskite films and fully assembled perovskite solar cell. Top-view SEM micrograph of (A) P + 0% $MAPbBr_3$ and (B) P + 5% $MAPbBr_3$, (C) and (D) schematic illustration showing the reduction in grain size upon introduction of $MAPbBr_3$, (E) top-view SEM micrograph of P + 20% $MAPbBr_3$, and (F) cross-sectional SEM micrograph of a (P + 5% $MAPbBr_3$)-based device.

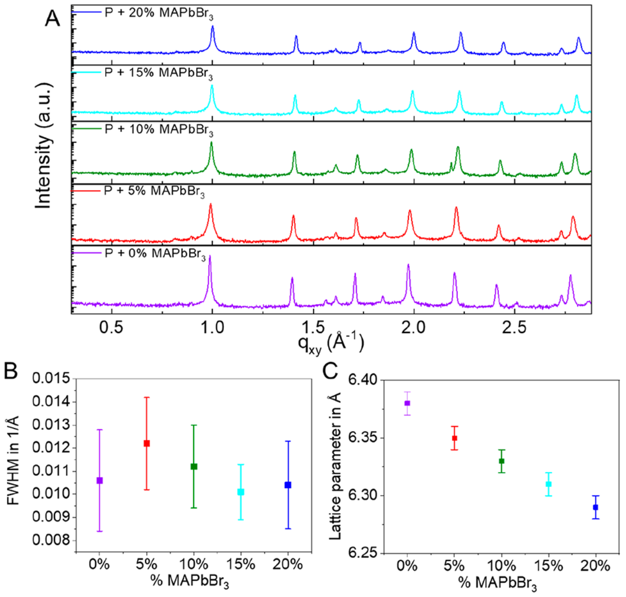

Figure 2. (A) Grazing-incidence X-ray diffraction patterns of the perovskite for different percentages of $MAPbBr_3$. (B) Average full width at half-maximum (fwhm) of the fitted perovskite peaks for different percentages of $MAPbBr_3$. The fwhm correlates with the size of the coherently scattering domains, which is not strongly affected by the amount of added $MAPbBr_3$. (C) Average cubic lattice parameter of the fitted perovskite for different $MAPbBr_3$ percentages.

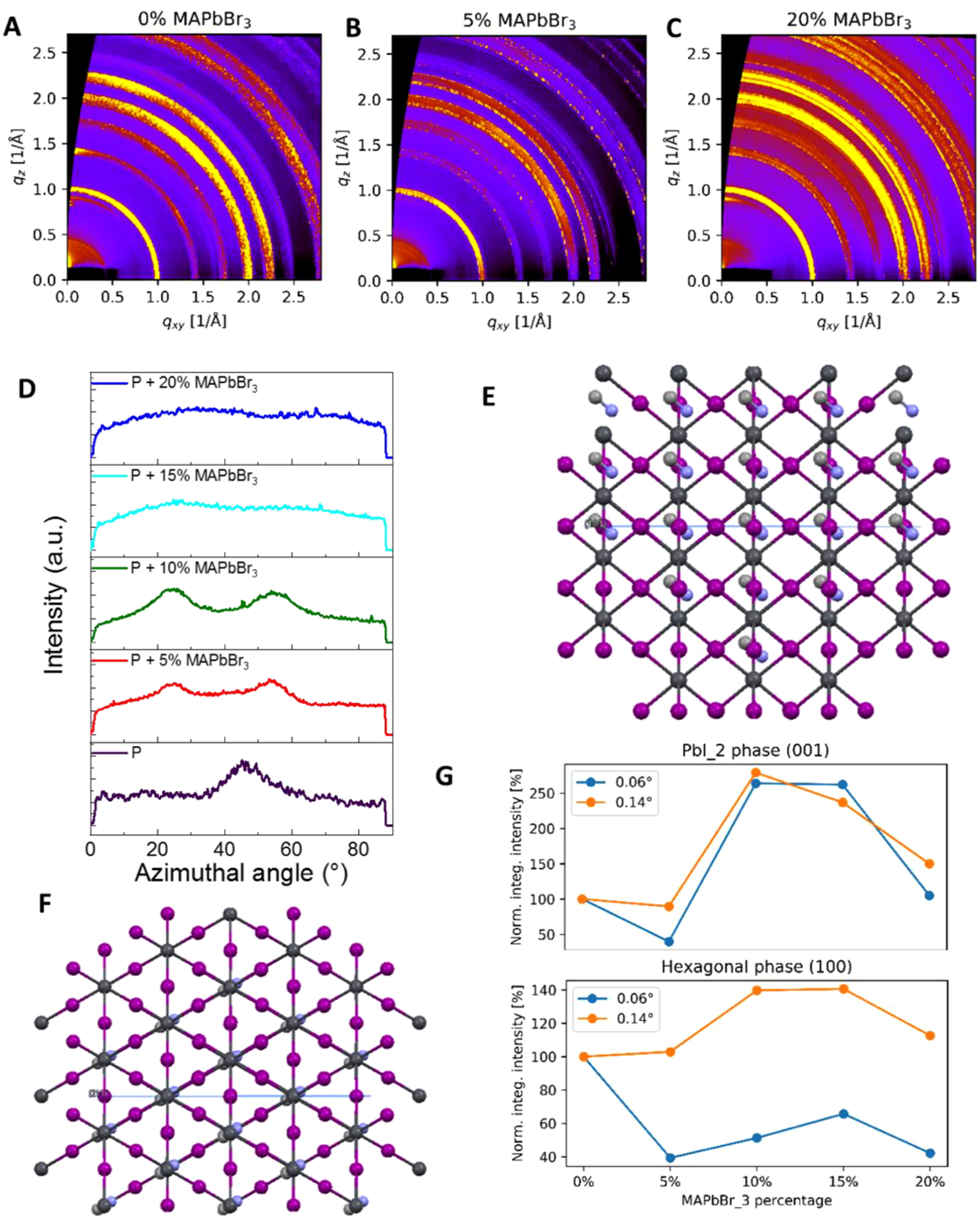

Figure 3. Reciprocal space maps obtained from GIWAXS of perovskite films with different amounts of MAPbBr$_3$ at an angle of incidence of 0.06° for (A) P + 0% MAPbBr$_3$, (B) P + 5% MAPbBr$_3$, and (C) P + 20% MAPbBr$_3$. (D) Radially integrated intensity plots along the ring at $q_z \approx 2$ Å^{-1} for the different perovskite compositions derived from the corresponding 2D-GIWAXS patterns. (E) Sketch of the ⟨111⟩ unit cell orientation for P-alternating layers of lead cations (gray) and I$^-$ anions (purple). (F) Sketch of the ⟨211⟩ unit cell orientation for P + 5% MAPbBr$_3$ and higher-alternating mixed layers, P = $CsI_{0.05}(FA_{1-y}MA_y)_{0.95}Pb(I_{1-y}Br_y)_3$. (G) Integrated intensity of the (001) and (100) Debye−Scherrer rings of PbI$_2$ and the hexagonal phase normalized to the perovskite (100) intensity for different percentages of MAPbBr$_3$ at an angle of incidence of 0.06° and 0.14°. The intensity is given relative to 0% MAPbBr$_3$.

MAPbBr$_3$, which is an intuitive result since MA$^+$ and Br$^-$ are both smaller than FA$^+$ and I$^-$, respectively (Figure S5).[31] The linear dependence is also in agreement with Vegard's law. From the peak width, we determine that the size of coherently scattering domains is on average at least ∼55 nm for all films, which means that the defect density in the crystal lattice is relatively low and not strongly reduced upon mixing.[32]

We performed grazing-incidence X-ray diffraction at different angles of incidence using an area detector. Figure 3A−C and Figure S6 show examples of the obtained reciprocal space maps (RSMs) for different perovskite films at an angle of incidence of 0.06°. By analyzing the azimuthal intensity distribution of the Debye−Scherrer rings, we observed that for different amounts of added MAPbBr$_3$, the preferred orientation of the perovskite crystallites differs with respect to the substrate plane. Figure 3D shows that for MAPbBr$_3$-free perovskite films, the angular distribution of the first Debye−Scherrer ring shows only one maximum at 45°. We analyzed the relative angles between the maxima of different diffraction rings and determined that the preferred orientation parallel to

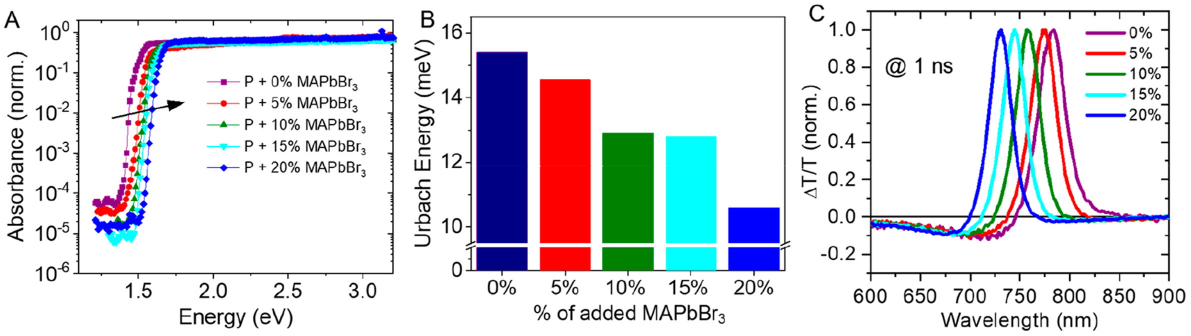

Figure 4. (A) Photothermal deflection absorption spectra of the perovskite with different amounts of MAPbBr$_3$. (B) Histograms of the Urbach energy measured on the different perovskite films. (C) Transient absorption spectrum at 1 ns representing different ground-state bleaches corresponding to a band edge of the perovskites.

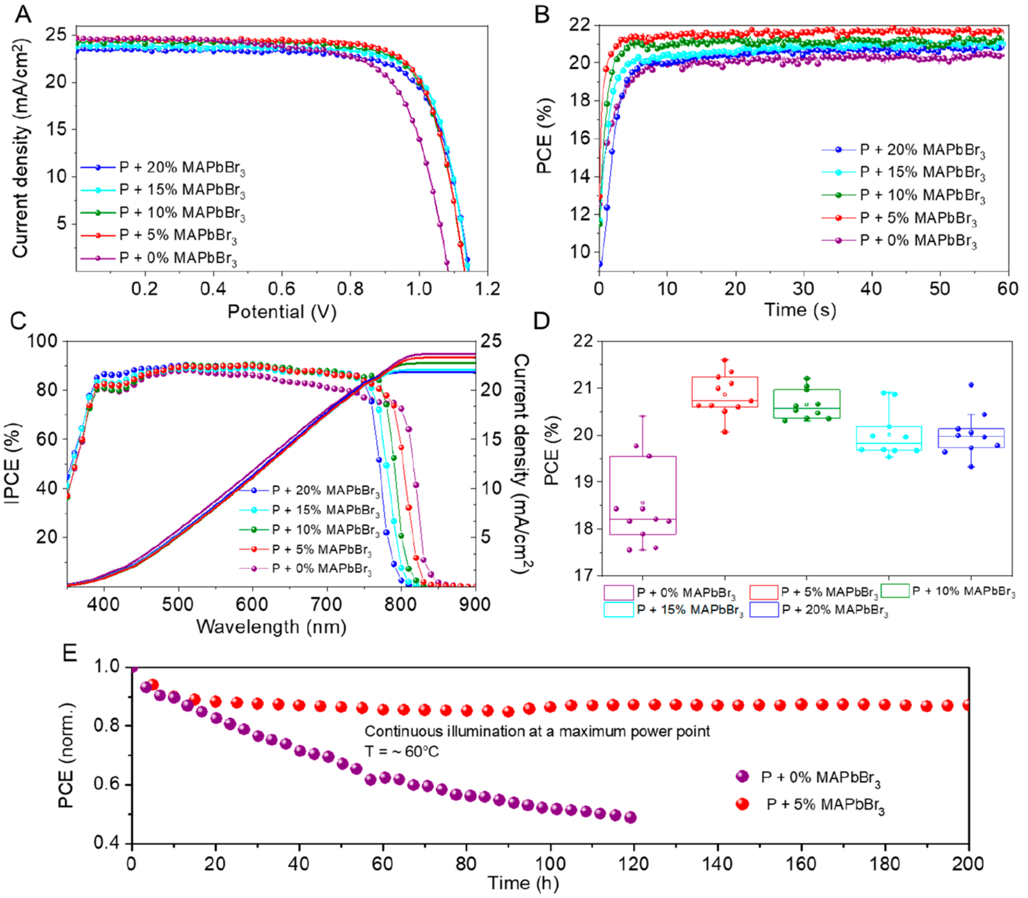

Figure 5. Photovoltaic characterization of devices based on different perovskite compositions (P + *y*% MAPbBr$_3$). (A) Current density−voltage (*J*−*V*) curves (reverse scan) recorded at a scan rate of 0.05 V/s under the irradiation of simulated AM 1.5G. (B) Maximum power point tracking for 60 s, yielding stabilized efficiencies summarized in Table 1. (C) IPCE spectra as a function of monochromatic wavelength recorded for different perovskite composition-based devices. Also shown are integrated current densities obtained from the respective IPCE spectrum. (D) Statistical analysis of the PCE for each perovskite composition. (E) Plot of the operational stability of an unencapsulated (P + 0% MAPbBr$_3$)- and (P + 5% MAPbBr$_3$)-based device examined at a maximum power point under continuous full-sun illumination at 60 °C in a nitrogen atmosphere.

the substrate plane is ⟨111⟩ (Figure 3E). Thus, we attribute the maximum in Figure 3A to the (100) plane.

With the addition of 5% MAPbBr$_3$, we observe that the angular intensity distribution of the first ring changes from a single maximum to two different maxima at 54° and 23° (Figure 3D, red trace). We determined that the preferred orientation parallel to the substrate is ⟨211⟩, and thus, we attribute the two maxima on the first ring to the (100) and (010)/(001) planes, respectively (Figure 3F). For the 10% MAPbBr$_3$ sample, this distribution becomes even narrower, but for amounts higher than 10%, we observe an almost homogeneous distribution, indicating that there is no preferred orientation of the perovskite crystallites. We further determined the relative amount of impurities in the samples, in particular, the photoinactive hexagonal phase and lead iodide, at different angles of incidence.

Figure 3G shows the integrated peak intensity of the PbI$_2$ (001) ring and the (100) ring of the hexagonal phase for

Table 1. Photovoltaic Parameters Extracted from the *J*−*V* Curves Corresponding to the Most Efficient PSCs for Each Perovskite Composition (P + *y*% $MAPbBr_3$) and Bandgap Values Estimated from IPCE Spectra

$MAPbBr_3$ conc (%)	J_{SC} (mA cm^{-2})	V_{OC} (V)	FF	PCE (%)	stabilized PCE (%)	IPCE onset (nm)	bandgap (eV)
0	25.45	1.090	0.727	20.4	20.1	843	1.487
5	24.69	1.126	0.768	21.6	21.4	829	1.503
10	24.13	1.131	0.768	21.2	21.0	811	1.537
15	23.61	1.135	0.777	20.9	20.7	803	1.546
20	23.29	1.156	0.765	20.8	20.6	795	1.572

different amounts of $MAPbBr_3$ at angles of incidence of 0.06° and 0.14° normalized to the perovskite (100) intensity. We observe that, overall, an increase of the $MAPbBr_3$ content leads to an increase of the amounts of the hexagonal phase as well as PbI_2 in the bulk except for a $MAPbBr_3$ content of 5%. However, near to the surface, we observe for a $MAPbBr_3$ content of 5% a strong reduction of the impurities to less than half compared to the case for pure $FAPbI_3$.

Therefore, we infer that by adding 5% of $MAPbBr_3$ to $FAPbI_3$, the number of phase impurities at the surface can be reduced, which might have an impact on the performance of the perovskite as an absorber material.[33] Furthermore, introducing more than 5% $MAPbBr_3$ seems to strongly increase the amount of PbI_2 in the sample both in the bulk and near to the top surface, which might also be detrimental to the photovoltaic performance.

The influence of $MAPbBr_3$ incorporation on the optoelectronic properties of mixed-halide perovskite films was investigated using PDS, a highly sensitive optical absorption measurement. With the introduction of $MAPbBr_3$ into $FAPbI_3$ perovskite lattice, the bandgap energy shifted toward higher energies (Figure 4A), which can be explained by considering the substitution of larger ions including FA^+ and I^- with smaller ions like MA^+ and Br^-. From the PDS spectrum, we measure an Urbach energy of 15.4 meV for the $FA_{0.95}Cs_{0.05}PbI_3$ film (Figure 4B). The Urbach energy arises through defects and structural disorder in the crystalline structure and thermal fluctuation of constituent atoms or ions.[34,35] When $MAPbBr_3$ is introduced into the CsI-containing $FAPbI_3$ lattice, the Urbach energy decreases systematically to 13 and 11 meV, respectively, for 10% and 20% compositions (Figure 4B), clearly establishing lower energetic disorder associated with the $MAPbBr_3$-containing films. Figure 4C shows the normalized transient absorption spectra at 1 ns acquired after the perovskite films were excited with a 500 nm pump pulse. The spectra consist of ground-state bleach ($\Delta T/T > 0$) centered around band edge and refractive index change ($\Delta T/T < 0$) above the bandgap. Increasing $MAPbBr_3$ content monotonically increases the bandgap, as evident from the blue shift of the ground-state bleach (GSB), consistent with the PDS data. The normalized decay dynamics (Figure S7) reveals that mixed-halide perovskite films exhibit slow GSB decay as compared to $MAPbBr_3$-free films. When 5% of $MAPbBr_3$ was added into the FA-dominant lattice, the charge-carrier lifetime increases remarkably exponentially from 10 to 100 ns. Interestingly, we do not observe any shift in the GSB with the delay in time, establishing that the films are phase pure, and ruling out any phase segregation. The full transient absorption contour maps (Figure S8) recorded for each perovskite film confirm the presence of long-lived charge carriers in $MAPbBr_3$-containing perovskite films further supported by time-resolved photoluminescence (Figure S9).[36] The relatively poor optoelectronic quality of bromide-free perovskite films could be due to the low-structural stability of the FA-dominant phase, which eventually renders them more prone to the formation of defects and energetic disorder.[37]

The introduction of $MAPbBr_3$ into the $FAPbI_3$ perovskite system should raise the bandgap and thus decrease the J_{SC} and/or increase the V_{OC}. As the PCE of a photovoltaic cell depends on both parameters, therefore, the best trade-off between high J_{SC} (low $MAPbBr_3$ content) and high V_{OC} (high $MAPbBr_3$ content) needs to be determined for different perovskite compositions. We investigated the photovoltaic performance of PSCs based on $CsI_{0.05}(FA_{1-y}MA_y)_{0.95}Pb(I_{1-y}Br_y)_3$ films using conventional n-i-p device architecture with a mesoporous TiO_2 layer as an electron transporting material (ETM) and spiro-OMeTAD as a hole transporting material (HTM). The *J*−*V* plots corresponding to the most efficient devices for each composition are displayed in Figure 5A, and the corresponding extracted *PV* parameters are summarized in Table 1. The bromide-free PSC yielded a J_{SC} of 25.4 mA cm^{-2}, a V_{OC} of 1.090 V, and a fill factor (FF) of 0.73, resulting in a PCE of 20.4%. However, the perovskite composition containing 5% $MAPbBr_3$ exhibits better photovoltaic performances with a PCE of 21.6% (J_{SC} = 24.7 mA cm^{-2}, V_{OC} = 1.126 V, and FF of 0.77), indicating this composition to be the best compromise between high photocurrent and high photovoltage among all the compositions. When the $MAPbBr_3$ content increases to 10%, the PCE drops to 21.2% and PSCs containing 15% $MAPbBr_3$ yielded a PCE = 20.9% closely followed by the 20% $MAPbBr_3$ perovskite composition, which showed a PCE = 20.8%. The relatively low photovoltage displayed by bromide-free PSC could be due to the less structural stability of the $MAPbBr_3$-free $FAPbI_3$ phase, which apparently leaves the film more susceptible to defects and trap states.[38,39] We further determined the stabilized (scan-speed independent) PCEs of these devices by probing at their maximum power point (MPP) under full-sun illumination for 60 s (Figure 5B), and the results are shown in Table 1. Remarkably, the stabilized PCEs measured with MPP-tracking are in excellent agreement to the values obtained via *J*−*V* measurements, suggesting low hysteretic behavior,[40] which is further supported by the *J*−*V* hysteresis measurements (Figure S10). From all these results, it is particularly interesting to note that the stabilized PCE values of the 5% $MAPbBr_3$ composition not only surpasses the performance of other PSCs but also is higher than that of state-of-the-art triple-cation PSCs (Figure S11).

The integrated photocurrent densities obtained from the incident photon-to-electron conversion efficiency (IPCE) spectra (Figure 5C) are in excellent agreement with those obtained from the *J*−*V* curves, indicating that the spectral mismatch between our simulator and AM-1.5 standard solar radiation is negligible. Furthermore, the sharp IPCE onset shifted from 843 to 829 nm after introducing 5% $MAPbBr_3$, as summarized together with J_{SC} and V_{OC} in Table 1 and vice versa. The photovoltaic results revealed that the higher the J_{SC}, the lower the V_{OC}. Interestingly, the perovskite composition containing 5% $MAPbBr_3$ shows the best trade-off between the J_{SC} and V_{OC}. To investigate the reproducibility of our results, which is a key factor for large-scale deployment of PSCs, it is crucial not only to look at the most efficient device for each composition but also to investigate the averaged PCE of several devices from different batches. Table S2 summarizes the averaged data of several cells of each composition ($n > 10$) from different batches and Figure 5D shows the PCE distribution for each composition. Evidently, 5% $MAPbBr_3$ shows a good reproducibility with an average PCE exceeding 21% while retaining the most efficient composition. The other $MAPbBr_3$-containing compositions displayed PCEs in the range 20−21%, whereas $MAPbBr_3$-free PSCs exhibit poor reproducibility, with PCEs ranging from 17.5% to 20%. The poor reproducibility of P + 0% $MAPbBr_3$ could be asserted with the inherent structural and thermodynamic instability of the $FAPbI_3$ system.[10]

Finally, to evaluate the long-term viability of these devices, the operational stability of devices (unencapsulated) was tested under continuous full-sun illumination at their MPP at 60 °C in an inert atmosphere (Figure 5E).[38,41] The PSCs containing 5% $MAPbBr_3$, demonstrated the best operational stability, which is comparable to that of state-of-the-art PSCs containing 17% $MAPbBr_3$ (Figure S12). In contrast, $MAPbBr_3$-free PSC exhibits a very poor operational stability, losing more than 50% of its initial PCE after 100 h, which underlines the crucial role of $MAPbBr_3$ toward stabilizing the $FAPbI_3$ system into the perovskite structure.[14] All $MAPbBr_3$-containing devices showed comparable and excellent operational stability.[42]

In summary, we demonstrate that the optoelectronic quality and structural stability of the $FAPbI_3$ films are strongly dependent on the presence and content of $MAPbBr_3$. Crucial guiding principles for designing stable and high-quality perovskite films exhibiting direct correlation with the solar cell performance have been put forth as (1) minimizing energetic disorder, (2) improving charge-carrier dynamics, and (3) reducing surface phase impurities. The introduction of $MAPbBr_3$ decreases the perovskite grain size by increasing the nucleation density, besides influencing the preferred orientation of perovskite grains. For $MAPbBr_3$-free system, the introduction of 5−10% $MAPbBr_3$ changes the preferred orientation from the (111) to (211) with respect to the substrate. Also, we find a strong reduction of the hexagonal nonperovskite phase for films with $MAPbBr_3$ compared to results for $MAPbBr_3$-free films at the top surface. Consequently, the introduction of $MAPbBr_3$ reduces the energetic disorder and prolongs the lifetime of photogenerated charge-carrier. Finally, by benefiting from the positive effects of $MAPbBr_3$ on the optoelectronic quality and structural stability, we obtained remarkable photovoltaic performance and excellent operational stability without sacrificing much of the light-harvesting properties of $FAPbI_3$. To further improve the performance of PSCs, we would need to increase the crystallinity of absorber layer exhibiting an optimal bandgap and minimize defect/trap states in the bulk and/or at the interfaces and parasitic recombination including nonradiative and interfacial recombination without compromising on the energetic or band alignment within a fully assembled device.[43,44] Fundamentally, the same set of rules could be extended to other perovskite systems. Arguably our comprehensive study will contribute to a fundamental understanding of PSCs and could help in designing new and stable light absorbers with tailored optoelectronic properties for efficient devices.

■ ASSOCIATED CONTENT

Supporting Information

The Supporting Information is available free of charge at https://pubs.acs.org/doi/10.1021/acs.jpclett.0c02791.

> Experimental section, XPS spectra, compositional analysis of perovskite films, SEM micrographs, reciprocal space maps, XRD peaks, the kinetics of ground-state bleach, full-contour TA maps, photoluminescence spectra, *J*−*V* hysteresis curves, photovoltaic parameters, operational stability plot with different amounts of $MAPbBr_3$. (PDF)

■ AUTHOR INFORMATION

Corresponding Author

M. Ibrahim Dar − *Cavendish Laboratory, Department of Physics, University of Cambridge, Cambridge CB3 0HE, United Kingdom; Laboratory of Photonics and Interfaces, Institute of Chemical Sciences and Engineering, École Polytechnique Fédérale de Lausanne, Lausanne CH-1015, Switzerland;* orcid.org/0000-0001-9489-8365; Email: id338@cam.ac.uk

Authors

Thomas Baumeler − *Laboratory of Photonics and Interfaces, Institute of Chemical Sciences and Engineering, École Polytechnique Fédérale de Lausanne, Lausanne CH-1015, Switzerland*

Neha Arora − *Cavendish Laboratory, Department of Physics, University of Cambridge, Cambridge CB3 0HE, United Kingdom; Laboratory of Photonics and Interfaces, Institute of Chemical Sciences and Engineering, École Polytechnique Fédérale de Lausanne, Lausanne CH-1015, Switzerland;* orcid.org/0000-0003-4068-3574

Alexander Hinderhofer − *Institut für Angewandte Physik, Universität Tübingen, 72076 Tübingen, Germany;* orcid.org/0000-0001-8152-6386

Seckin Akin − *Laboratory of Photonics and Interfaces, Institute of Chemical Sciences and Engineering, École Polytechnique Fédérale de Lausanne, Lausanne CH-1015, Switzerland; Department of Metallurgical and Materials Engineering, Karamanoglu Mehmetbey University, 70100 Karaman, Turkey;* orcid.org/0000-0001-9852-7246

Alessandro Greco − *Institut für Angewandte Physik, Universität Tübingen, 72076 Tübingen, Germany;* orcid.org/0000-0002-3714-7941

Mojtaba Abdi-Jalebi − *Cavendish Laboratory, Department of Physics, University of Cambridge, Cambridge CB3 0HE, United Kingdom;* orcid.org/0000-0002-9430-6371

Ravichandran Shivanna − *Cavendish Laboratory, Department of Physics, University of Cambridge, Cambridge CB3 0HE, United Kingdom;* orcid.org/0000-0002-0915-6066

Ryusuke Uchida − *Laboratory of Photonics and Interfaces, Institute of Chemical Sciences and Engineering, École Polytechnique Fédérale de Lausanne, Lausanne CH-1015, Switzerland; Institute for Energy and Material/Food*

Resources, Technology Innovation Division, Panasonic Corporation, Osaka 570-8501, Japan

Yuhang Liu – *Laboratory of Photonics and Interfaces, Institute of Chemical Sciences and Engineering, École Polytechnique Fédérale de Lausanne, Lausanne CH-1015, Switzerland*

Frank Schreiber – *Institut für Angewandte Physik, Universität Tübingen, 72076 Tübingen, Germany;* orcid.org/0000-0003-3659-6718

Shaik M. Zakeeruddin – *Laboratory of Photonics and Interfaces, Institute of Chemical Sciences and Engineering, École Polytechnique Fédérale de Lausanne, Lausanne CH-1015, Switzerland*

Richard H. Friend – *Cavendish Laboratory, Department of Physics, University of Cambridge, Cambridge CB3 0HE, United Kingdom;* orcid.org/0000-0001-6565-6308

Michael Graetzel – *Laboratory of Photonics and Interfaces, Institute of Chemical Sciences and Engineering, École Polytechnique Fédérale de Lausanne, Lausanne CH-1015, Switzerland;* orcid.org/0000-0002-0068-0195

Complete contact information is available at:
https://pubs.acs.org/10.1021/acs.jpclett.0c02791

Author Contributions

M.I.D. conceived the idea of the work and designed the project. T.B. together with S.A., R.U., and N.A. fabricated the devices. T.B., M.I.D., N.A., and S.M.Z. characterized the devices. T.B. and M.I.D. analyzed the XPS data. M.I.D. and T.B conducted and analyzed the stability tests with contributions from Y.L. M.I.D. acquired and analyzed the SEM data. A.H., A.G., M.I.D., and F.S. performed, analyzed, and discussed the XRD data. M.A.-J. performed PDS experiments and M.A.-J., M.I.D., and R.H.F. analyzed and discussed the PDS results. R.S. carried out the TA experiments, and R.S. and R.H.F. analyzed and discussed the TA results. M.I.D supervised the study with M.G. M.I.D. wrote the manuscript together with T.B. and N.A., and all the authors discussed the results and contributed toward finalizing the draft.

Notes

The authors declare no competing financial interest.

■ ACKNOWLEDGMENTS

M.I.D. acknowledges support from the Royal Society (grant no. URF\R1\201696). T.B. acknowledges support from the Swiss National Science Foundation (project no. IZJSZ2_180176). N.A. and R.H.F. acknowledge support from the GCRF/EPSRC SUNRISE (EP/P032591/1) project. We thank the European Synchrotron Radiation Facility (ESRF) for provision of synchrotron radiation and A. Chumakov and F. Zontone for assistance in using beamline ID10. We thank P. Mettraux (Molecular and Hybrid Materials Characterization Center, EPFL) for carrying out XPS measurements. We thank G. Jacopin for TRPL measurements. S.A. thanks TUBITAK-2214-A International Doctoral Research Fellowship Programme, for supporting his research at EPFL. M.A.-J. thanks Cambridge Materials Limited, Wolfson College, University of Cambridge and EPSRC (grant no. EP/M005143/1) for their funding and technical support.

■ REFERENCES

(1) Kojima, A.; Teshima, K.; Shirai, Y.; Miyasaka, T. Organometal Halide Perovskites as Visible-Light Sensitizers for Photovoltaic Cells. *J. Am. Chem. Soc.* **2009**, *131* (17), 6050–6051.

(2) Lee, M. M.; Teuscher, J.; Miyasaka, T.; Murakami, T. N.; Snaith, H. J. Efficient Hybrid Solar Cells Based on Meso-Superstructured Organometal Halide Perovskites. *Science* **2012**, *338* (6107), 643.

(3) Kim, H.-S.; Lee, C.-R.; Im, J.-H.; Lee, K.-B.; Moehl, T.; Marchioro, A.; Moon, S.-J.; Humphry-Baker, R.; Yum, J.-H.; Moser, J. E.; et al. Lead Iodide Perovskite Sensitized All-Solid-State Submicron Thin Film Mesoscopic Solar Cell with Efficiency Exceeding 9%. *Sci. Rep.* **2012**, *2*, 591.

(4) Dar, M. I.; Jacopin, G.; Meloni, S.; Mattoni, A.; Arora, N.; Boziki, A.; Zakeeruddin, S. M.; Rothlisberger, U.; Grätzel, M. Origin of Unusual Bandgap Shift and Dual Emission in Organic-Inorganic Lead Halide Perovskites. *Sci. Adv.* **2016**, *2* (10), No. e1601156.

(5) Xing, G.; Mathews, N.; Lim, S. S.; Yantara, N.; Liu, X.; Sabba, D.; Grätzel, M.; Mhaisalkar, S.; Sum, T. C. Low-Temperature Solution-Processed Wavelength-Tunable Perovskites for Lasing. *Nat. Mater.* **2014**, *13*, 476.

(6) Stoumpos, C. C.; Malliakas, C. D.; Kanatzidis, M. G. Semiconducting Tin and Lead Iodide Perovskites with Organic Cations: Phase Transitions, High Mobilities, and Near-Infrared Photoluminescent Properties. *Inorg. Chem.* **2013**, *52* (15), 9019–9038.

(7) Dong, Q.; Fang, Y.; Shao, Y.; Mulligan, P.; Qiu, J.; Cao, L.; Huang, J. Electron-Hole Diffusion Lengths > 175 μm in Solution-Grown $CH_3NH_3PbI_3$ Single Crystals. *Science* **2015**, *347* (6225), 967–970.

(8) Manser, J. S.; Christians, J. A.; Kamat, P. V. Intriguing Optoelectronic Properties of Metal Halide Perovskites. *Chem. Rev.* **2016**, *116* (21), 12956–13008.

(9) Noh, J. H.; Im, S. H.; Heo, J. H.; Mandal, T. N.; Seok, S. I. Chemical Management for Colorful, Efficient, and Stable Inorganic–Organic Hybrid Nanostructured Solar Cells. *Nano Lett.* **2013**, *13* (4), 1764–1769.

(10) Koh, T. M.; Fu, K.; Fang, Y.; Chen, S.; Sum, T. C.; Mathews, N.; Mhaisalkar, S. G.; Boix, P. P.; Baikie, T. Formamidinium-Containing Metal-Halide: An Alternative Material for Near-IR Absorption Perovskite Solar Cells. *J. Phys. Chem. C* **2014**, *118* (30), 16458–16462.

(11) Jeong, M.; Choi, I. W.; Go, E. M.; Cho, Y.; Kim, M.; Lee, B.; Jeong, S.; Jo, Y.; Choi, H. W.; Lee, J.; et al. Stable Perovskite Solar Cells with Efficiency Exceeding 24.8% and 0.3-V Voltage Loss. *Science* **2020**, *369* (6511), 1615.

(12) Liu, Y.; Akin, S.; Hinderhofer, A.; Eickemeyer, F. T.; Zhu, H.; Seo, J.-Y.; Zhang, J.; Schreiber, F.; Zhang, H.; Zakeeruddin, S. M.; et al. Stabilization of Highly Efficient and Stable Phase-Pure $FAPbI_3$ Perovskite Solar Cells by Molecularly Tailored 2D-Overlayers. *Angew. Chem., Int. Ed.* **2020**, *59* (36), 15688–15694.

(13) Pellet, N.; Gao, P.; Gregori, G.; Yang, T.-Y.; Nazeeruddin, M. K.; Maier, J.; Grätzel, M. Mixed-Organic-Cation Perovskite Photovoltaics for Enhanced Solar-Light Harvesting. *Angew. Chem., Int. Ed.* **2014**, *53* (12), 3151–3157.

(14) Jeon, N. J.; Noh, J. H.; Yang, W. S.; Kim, Y. C.; Ryu, S.; Seo, J.; Seok, S. I. Compositional Engineering of Perovskite Materials for High-Performance Solar Cells. *Nature* **2015**, *517*, 476.

(15) Saliba, M.; Matsui, T.; Domanski, K.; Seo, J.-Y.; Ummadisingu, A.; Zakeeruddin, S. M.; Correa-Baena, J.-P.; Tress, W. R.; Abate, A.; Hagfeldt, A.; et al. Incorporation of Rubidium Cations into Perovskite Solar Cells Improves Photovoltaic Performance. *Science* **2016**, *354* (6309), 206.

(16) Uchida, R.; Binet, S.; Arora, N.; Jacopin, G.; Alotaibi, M. H.; Taubert, A.; Zakeeruddin, S. M.; Dar, M. I.; Graetzel, M. Insights about the Absence of Rb Cation from the 3D Perovskite Lattice: Effect on the Structural, Morphological, and Photophysical Properties and Photovoltaic Performance. *Small* **2018**, *14* (36), 1802033.

(17) Yadav, P.; Dar, M. I.; Arora, N.; Alharbi, E. A.; Giordano, F.; Zakeeruddin, S. M.; Grätzel, M. The Role of Rubidium in Multiple-

Cation-Based High-Efficiency Perovskite Solar Cells. *Adv. Mater.* **2017**, *29* (40), 1701077.

(18) Abdi-Jalebi, M.; Andaji-Garmaroudi, Z.; Cacovich, S.; Stavrakas, C.; Philippe, B.; Richter, J. M.; Alsari, M.; Booker, E. P.; Hutter, E. M.; Pearson, A. J.; et al. Maximizing and Stabilizing Luminescence from Halide Perovskites with Potassium Passivation. *Nature* **2018**, *555*, 497.

(19) Liu, Y.; Akin, S.; Pan, L.; Uchida, R.; Arora, N.; Milić, J. V.; Hinderhofer, A.; Schreiber, F.; Uhl, A. R.; Zakeeruddin, S. M.; et al. Ultrahydrophobic 3D/2D Fluoroarene Bilayer-Based Water-Resistant Perovskite Solar Cells with Efficiencies Exceeding 22%. *Sci. Adv.* **2019**, *5* (6), No. eaaw2543.

(20) Lee, J.-W.; Dai, Z.; Han, T.-H.; Choi, C.; Chang, S.-Y.; Lee, S.-J.; De Marco, N.; Zhao, H.; Sun, P.; Huang, Y.; et al. 2D Perovskite Stabilized Phase-Pure Formamidinium Perovskite Solar Cells. *Nat. Commun.* **2018**, *9* (1), 3021.

(21) Saidaminov, M. I.; Kim, J.; Jain, A.; Quintero-Bermudez, R.; Tan, H.; Long, G.; Tan, F.; Johnston, A.; Zhao, Y.; Voznyy, O.; et al. Suppression of Atomic Vacancies via Incorporation of Isovalent Small Ions to Increase the Stability of Halide Perovskite Solar Cells in Ambient Air. *Nat. Energy* **2018**, *3* (8), 648−654.

(22) Zhao, Y.; Tan, H.; Yuan, H.; Yang, Z.; Fan, J. Z.; Kim, J.; Voznyy, O.; Gong, X.; Quan, L. N.; Tan, C. S.; et al. Perovskite Seeding Growth of Formamidinium-Lead-Iodide-Based Perovskites for Efficient and Stable Solar Cells. *Nat. Commun.* **2018**, *9* (1), 1607.

(23) Min, H.; Kim, M.; Lee, S.-U.; Kim, H.; Kim, G.; Choi, K.; Lee, J. H.; Seok, S. I. Efficient, Stable Solar Cells by Using Inherent Bandgap of α-Phase Formamidinium Lead Iodide. *Science* **2019**, *366* (6466), 749−753.

(24) Zheng, X.; Hou, Y.; Bao, C.; Yin, J.; Yuan, F.; Huang, Z.; Song, K.; Liu, J.; Troughton, J.; Gasparini, N.; et al. Managing Grains and Interfaces via Ligand Anchoring Enables 22.3%-Efficiency Inverted Perovskite Solar Cells. *Nat. Energy* **2020**, *5* (2), 131−140.

(25) Saliba, M.; Matsui, T.; Seo, J.-Y.; Domanski, K.; Correa-Baena, J.-P.; Nazeeruddin, M. K.; Zakeeruddin, S. M.; Tress, W.; Abate, A.; Hagfeldt, A.; et al. Cesium-Containing Triple Cation Perovskite Solar Cells: Improved Stability, Reproducibility and High Efficiency. *Energy Environ. Sci.* **2016**, *9* (6), 1989−1997.

(26) Lee, J.-W.; Kim, D.-H.; Kim, H.-S.; Seo, S.-W.; Cho, S. M.; Park, N.-G. Formamidinium and Cesium Hybridization for Photo- and Moisture-Stable Perovskite Solar Cell. *Adv. Energy Mater.* **2015**, *5* (20), 1501310.

(27) Briggs, D.; Seah, M. P. *Practical Surface Analysis*, 2nd ed.; John Wiley: New York, 1996; *Vol. 1*.

(28) Pederson, L. R. Two-Dimensional Chemical-State Plot for Lead using XPS. *J. Electron Spectrosc. Relat. Phenom.* **1982**, *28* (2), 203−209.

(29) Bagus, P. S.; Illas, F.; Pacchioni, G.; Parmigiani, F. Mechanisms Responsible for Chemical Shifts of Core-Level Binding Energies and their Relationship to Chemical Bonding. *J. Electron Spectrosc. Relat. Phenom.* **1999**, *100* (1), 215−236.

(30) Dar, M. I.; Hinderhofer, A.; Jacopin, G.; Belova, V.; Arora, N.; Zakeeruddin, S. M.; Schreiber, F.; Grätzel, M. Function Follows Form: Correlation between the Growth and Local Emission of Perovskite Structures and the Performance of Solar Cells. *Adv. Funct. Mater.* **2017**, *27* (26), 1701433.

(31) Amat, A.; Mosconi, E.; Ronca, E.; Quarti, C.; Umari, P.; Nazeeruddin, M. K.; Grätzel, M.; De Angelis, F. Cation-Induced Band-Gap Tuning in Organohalide Perovskites: Interplay of Spin−Orbit Coupling and Octahedra Tilting. *Nano Lett.* **2014**, *14* (6), 3608−3616.

(32) Jones, T. W.; Osherov, A.; Alsari, M.; Sponseller, M.; Duck, B. C.; Jung, Y.-K.; Settens, C.; Niroui, F.; Brenes, R.; Stan, C. V.; et al. Lattice Strain Causes Non-Radiative Losses in Halide Perovskites. *Energy Environ. Sci.* **2019**, *12* (2), 596−606.

(33) Ball, J. M.; Petrozza, A. Defects in Perovskite-Halides and their Effects in Solar Cells. *Nat. Energy* **2016**, *1* (11), 16149.

(34) Abdi-Jalebi, M.; Dar, M. I.; Sadhanala, A.; Senanayak, S. P.; Franckevičius, M.; Arora, N.; Hu, Y.; Nazeeruddin, M. K.; Zakeeruddin, S. M.; Grätzel, M.; et al. Impact of Monovalent Cation Halide Additives on the Structural and Optoelectronic Properties of $CH_3NH_3PbI_3$ Perovskite. *Adv. Energy Mater.* **2016**, *6* (10), 1502472.

(35) Arora, N.; Dar, M. I.; Abdi-Jalebi, M.; Giordano, F.; Pellet, N.; Jacopin, G.; Friend, R. H.; Zakeeruddin, S. M.; Grätzel, M. Intrinsic and Extrinsic Stability of Formamidinium Lead Bromide Perovskite Solar Cells Yielding High Photovoltage. *Nano Lett.* **2016**, *16* (11), 7155−7162.

(36) Shi, D.; Adinolfi, V.; Comin, R.; Yuan, M.; Alarousu, E.; Buin, A.; Chen, Y.; Hoogland, S.; Rothenberger, A.; Katsiev, K.; et al. Low Trap-State Density and Long Carrier Diffusion in Organolead Trihalide Perovskite Single Crystals. *Science* **2015**, *347* (6221), 519−522.

(37) Yang, Z.; Chueh, C.-C.; Liang, P.-W.; Crump, M.; Lin, F.; Zhu, Z.; Jen, A. K. Y. Effects of Formamidinium and Bromide Ion Substitution in Methylammonium Lead Triiodide toward High-Performance Perovskite Solar Cells. *Nano Energy* **2016**, *22*, 328−337.

(38) Zhang, Y.; Zhou, Z.; Ji, F.; Li, Z.; Cui, G.; Gao, P.; Oveisi, E.; Nazeeruddin, M. K.; Pang, S. Trash into Treasure: δ-$FAPbI_3$ Polymorph Stabilized $MAPbI_3$ Perovskite with Power Conversion Efficiency beyond 21%. *Adv. Mater.* **2018**, *30* (22), 1707143.

(39) Niu, T.; Lu, J.; Tang, M.-C.; Barrit, D.; Smilgies, D.-M.; Yang, Z.; Li, J.; Fan, Y.; Luo, T.; McCulloch, I.; et al. High Performance Ambient-Air-Stable $FAPbI_3$ Perovskite Solar Cells with Molecule-Passivated Ruddlesden−Popper/3D Heterostructured Film. *Energy Environ. Sci.* **2018**, *11* (12), 3358−3366.

(40) Eames, C.; Frost, J. M.; Barnes, P. R. F.; O'Regan, B. C.; Walsh, A.; Islam, M. S. Ionic Transport in Hybrid Lead Iodide Perovskite Solar Cells. *Nat. Commun.* **2015**, *6* (1), 7497.

(41) Arora, N.; Dar, M. I.; Hinderhofer, A.; Pellet, N.; Schreiber, F.; Zakeeruddin, S. M.; Grätzel, M. Perovskite Solar Cells with CuSCN Hole Extraction Layers Yield Stabilized Efficiencies greater than 20%. *Science* **2017**, *358* (6364), 768.

(42) Christians, J. A.; Schulz, P.; Tinkham, J. S.; Schloemer, T. H.; Harvey, S. P.; Tremolet de Villers, B. J.; Sellinger, A.; Berry, J. J.; Luther, J. M. Tailored Interfaces of Unencapsulated Perovskite Solar Cells for > 1,000 h Operational Stability. *Nat. Energy* **2018**, *3* (1), 68−74.

(43) Akin, S.; Arora, N.; Zakeeruddin, S. M.; Grätzel, M.; Friend, R. H.; Dar, M. I. New Strategies for Defect Passivation in High-Efficiency Perovskite Solar Cells. *Adv. Energy Mater.* **2020**, *10* (13), 1903090.

(44) Saliba, M. Polyelemental Multicomponent Perovskite Semiconductor Libraries through Combinatorial Screening. *Adv. Energy Mater.* **2019**, *9* (25), 1803754.

https://dx.doi.org/10.1021/acs.jpclett.0c02791
J. Phys. Chem. Lett. 2020, 11, 10188−10195